

# Topological Phase Transitions in Kagome Ferromagnets: The Role of Intrinsic Rashba Spin-Orbit Coupling

Ritwik Das,\* Arkamitra Sen, and Indra Dasgupta†

*School of Physical Sciences, Indian Association for the Cultivation of Science  
2A and 2B Raja S.C. Mullick Road, Jadavpur, Kolkata 700 032, India*

(Dated: February 11, 2025)

The theoretically predicted Chern insulators have highlighted the potential of easy-axis kagome ferromagnets to host the quantum anomalous Hall effect. This phenomenon can also emerge from in-plane ferromagnetism in kagome systems via the breaking of both out-of-plane and in-plane mirror symmetries. In this paper, we demonstrate that the interplay between magnetism and mirror symmetries makes ferromagnetic kagome systems a versatile platform for realizing nontrivial topological phases, with the orientation of magnetic moments  $\hat{m}(\theta, \phi)$  at lattice sites serving as a key tuning parameter. We show that the Rashba spin-orbit coupling (SOC) induced by broken out-of-plane mirror symmetry together with the intrinsic SOC incorporated in a tight-binding model captures the rich topological phase diagram of kagome systems as a function of  $\hat{m}(\theta, \phi)$ . In particular, the restoration of in-plane mirror symmetry for specific values of  $\phi$  promotes topological phase transition upon variation of in-plane orientation of the moments  $\hat{m}(\theta = 90^\circ, \phi)$ . However the topological phase transition for the variation of  $\hat{m}(\theta, \phi = \text{constant})$  is dictated by a competition between Rashba SOC and intrinsic SOC. Density functional theory calculations for the ferromagnetic kagome monolayer  $\text{Co}_3\text{Pb}_3\text{S}_2$ , a representative compound belonging to the family  $\text{Co}_3\text{X}_3\text{Y}_2$  (X=Sn, Pb; Y=S, Se) further corroborate our predictions based on the proposed tight-binding model.

*Introduction.*—Magnetic kagome materials, with their unique geometry and exceptional electronic properties, offer a promising platform for exploring topological phases arising from the interplay between magnetism and topology<sup>1–3</sup>. Kagome ferromagnets, in particular, are intriguing due to their potential to host Chern insulating phases with dissipationless conducting edge states, making them viable candidates for spintronics and quantum computing applications<sup>4,5</sup>. Specifically, in two-dimensional (2D) monolayers, spin-orbit coupling (SOC) may induce band inversion, while ferromagnetic ordering breaks time-reversal symmetry (TRS)—that may give rise to the quantum anomalous Hall effect (QAHE), characterized by a non-zero Chern number, corresponding to the number of conducting edge states<sup>6–8</sup>. The electronic dispersion for kagome lattice geometry, in addition to supporting flat bands, features Dirac points at the Brillouin zone (BZ) corners, analogous to the honeycomb lattice, promoting Chern insulating phases similar to the Haldane model<sup>9</sup>.

Recent studies on honeycomb systems have demonstrated that both out-of-plane and in-plane ferromagnetism can induce Chern insulating phases, leading to a rich topological phase diagram that is tunable by the orientation of magnetic moments<sup>10–15</sup>. While theoretical models suggest that in-plane ferromagnetism can drive nontrivial Chern insulating phases with broken both out-of-plane and in-plane mirror symmetries, similar phases and consequent topological phase transitions (TPT) in kagome in-plane ferromagnets have remained largely unexplored<sup>3,16</sup>. The breaking and preservation of

mirror symmetries are critical for TPT in these systems.

In this paper, we develop a nearest-neighbor tight-binding (TB) model that incorporates broken out-of-plane mirror symmetry to capture Chern insulating phases for in-plane ferromagnetic kagome systems. SOC terms are introduced using semiclassical arguments while preserving the symmetry of the system. This model successfully reproduces key topological properties, including TPT driven by variations of the orientation of in-plane magnetic moments ( $\hat{m}(\theta = 90^\circ, \phi)$ ). While such Chern insulators in honeycomb systems typically exhibit Chern numbers  $C = \pm 1$ , kagome systems can support higher Chern numbers, such as  $C = \pm 2$  for specific bands. Additionally, the model also predicts TPT for the out-of-plane orientation of magnetic moments  $\hat{m}(\theta, \phi = \text{constant})$ , where the bands may have a larger Chern numbers  $C = \pm 3$ . Using first-principles electronic structure calculations within density functional theory (DFT), we demonstrate that the topological features predicted by this TB-model can be realised in insulating ferromagnetic monolayer  $\text{Co}_3\text{Pb}_3\text{S}_2$ , a representative compound from the family  $\text{Co}_3\text{X}_3\text{Y}_2$  (X=Sn, Pb; Y=S, Se) while their bulk counterpart, specifically the ferromagnetic Weyl semimetal  $\text{Co}_3\text{Sn}_2\text{S}_2$  also show magnetization tunable topological properties<sup>17,18</sup>.

*Symmetries and construction of a tight-binding model.*—We first examine the symmetries and geometry, in order to include the relevant terms in the proposed TB model. Figure 1(a) illustrates the kagome lattice with broken out-of-plane mirror symmetry (mirror residing in the kagome plane) due to surrounding elements. The in-plane mirrors are indicated by grey dotted lines in the figure, are perpendicular to the kagome plane.

To incorporate the kagome geometry in the TB model, the first nearest-neighbor hopping terms are considered,

\* intrd@iacs.res.in

† sspid@iacs.res.in

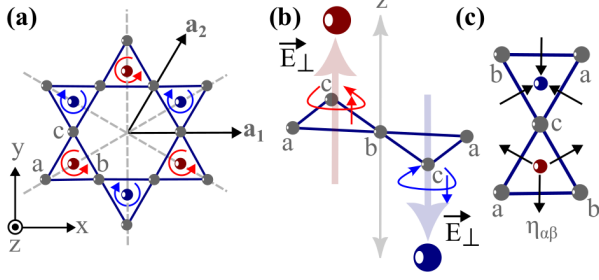


FIG. 1. Kagome lattice geometry. **(a)** The kagome lattice with in-plane mirrors (grey dotted lines). Blue and red arrows indicate favored paths due to intrinsic SOC for electron spins with up and down polarization, respectively. The surrounding elements above (red) and below (blue) to the kagome plane break the out-of-plane mirror symmetry. **(b)** Schematic of the intrinsic Rashba SOC effect. **(c)** Directional convention used for  $\vec{\eta}_{\alpha\beta}$  in the intrinsic Rashba SOC term of the TB model.

which generates three doubly degenerate bands as expected for a kagome system. An on-site field term is included to account for the ferromagnetic order and the direction of moments thereby lifting spin degeneracy and yielding a six-band manifold. However, without SOC, the orientation of moment does not affect the physical properties of the system.

To understand the influence of SOC on the topology of the system, it is crucial to examine the mirror symmetries and their impact on SOC-induced QAHE. The presence of mirror symmetry leads to vanishing Hall conductivity in 2D systems<sup>19</sup>. Also, magnetic moments parallel (perpendicular) to the mirror plane reverse (preserve) their directions and behave as a pseudo-vector<sup>20</sup>. Further, the out-of-plane mirror symmetry  $\hat{M}_z(x, y, z \rightarrow x, y, -z)$  is broken either by buckling or by surrounding elements (see Fig. 1(a) and (b))<sup>15</sup>.

Semiclassically, these out-of-plane surrounding elements generate an electric field  $\vec{E}$  with two components: one parallel to the kagome plane ( $\vec{E}_{\parallel}$ ) and another perpendicular to it ( $\vec{E}_{\perp}$ ) (see Fig. 1(b)). When an electron hops between nearest neighbor kagome sites, its velocity  $\vec{v}$  couples with  $\vec{E}$  to produce an effective magnetic field  $\vec{B}_{\text{eff}} \propto \vec{v} \times \vec{E}$ , which interacts with the spin of the electron, leading to an effective SOC Hamiltonian  $\hat{H}_{\text{SOC}} = -\vec{\sigma} \cdot \vec{B}_{\text{eff}}$ <sup>15</sup>.

The possible SOC terms in the TB model can be understood from this mechanism: the SOC term originating from  $\vec{E}_{\parallel}$  represents the intrinsic SOC (I-SOC), while the SOC term arising from  $\vec{E}_{\perp}$  corresponds to the intrinsic Rashba SOC (R-SOC). For the I-SOC term, the effective magnetic field  $\vec{B}_{\text{eff}}$  is perpendicular to the kagome plane, while for the R-SOC, set of  $\vec{\eta}_{\alpha\beta}$  vectors parallel to the kagome plane, associated with each nearest-neighbor bond (see Fig. 1(c)), defines the direction of  $\vec{B}_{\text{eff}}$ . The R-SOC term survives only in the absence of out-of-plane

mirror symmetry  $\hat{M}_z$ .

Considering all these terms, we construct the following TB model<sup>21-23</sup>:

$$\begin{aligned} \hat{H} = & -t \sum_{\langle i\alpha\gamma, j\beta\gamma \rangle} c_{i\alpha\gamma}^\dagger c_{j\beta\gamma} + B \sum_{i\alpha\gamma\delta} c_{i\alpha\gamma}^\dagger (\hat{m}(\theta, \phi) \cdot \vec{\sigma})_{\gamma\delta} c_{i\alpha\delta} \\ & + it_I \sum_{\langle i\alpha\gamma, j\beta\delta \rangle} \mu_{\alpha\beta} c_{i\alpha\gamma}^\dagger (\sigma_z)_{\gamma\delta} c_{j\beta\delta} \\ & + it_R \sum_{\langle i\alpha\gamma, j\beta\delta \rangle} \nu_{\alpha\beta} c_{i\alpha\gamma}^\dagger (\vec{\sigma} \cdot \vec{\eta}_{\alpha\beta})_{\gamma\delta} c_{j\beta\delta}. \end{aligned} \quad (1)$$

Here,  $\alpha, \beta$  are basis indices of the kagome lattice ( $|a\rangle, |b\rangle$  and  $|c\rangle$ ), and  $\gamma, \delta$  represent the spin indices ( $|\uparrow\rangle$  and  $|\downarrow\rangle$ ) (see Fig. 1). The second term corresponds to ferromagnetism, where  $B$  represents the magnitude and  $\hat{m}(\theta, \phi)$  is the direction of the magnetic moment. The components of  $\vec{\sigma}$  are the three Pauli matrices. The third and fourth terms correspond to the Kane-Mele type I-SOC<sup>24</sup> and R-SOC, respectively. The coefficients  $\mu_{\alpha\beta}$  and  $\nu_{\alpha\beta}$  take values of  $\pm 1$ , reflecting the two possible directions of electron velocities along the nearest-neighbor bonds. Depending on these signs, either clockwise or counterclockwise hopping becomes energetically favorable for spin-up or spin-down electrons, respectively.

For easy-axis ferromagnetism, where the moments are aligned perpendicular to the kagome plane and only breaks in-plane mirror symmetry, the first three terms of the Hamiltonian considered together, breaks TRS ( $\hat{\Theta}$ ) but preserve both inversion symmetry ( $\hat{I}$ ) and out-of-plane mirror symmetry ( $\hat{M}_z$ ). As a result, the combined symmetry  $\hat{\Theta} \otimes \hat{M}_z$ , which makes the Berry curvature  $\vec{\Omega}(\vec{k})$  an odd function within the first BZ, is broken, leading to a nonzero Chern number  $C$ . Similarly, the combined symmetry  $\hat{\Theta} \otimes \hat{M}_z \otimes \hat{I}$ , which causes the Berry curvature to vanish at each  $k$ -point, is also broken, resulting in a nonzero  $C$ . In contrast, for in-plane moment alignment  $\hat{m}(\theta = 90^\circ, \phi)$ , the first three terms break both  $\hat{\Theta}$  and  $\hat{M}_z$ , preventing non-trivial topology. However, the R-SOC term preserves  $\hat{\Theta}$  and  $\hat{I}$  while breaking  $\hat{M}_z$ , thereby introducing non-trivial topology for in-plane ferromagnetism<sup>11</sup>.

*Topological properties of the tight-binding model.*— The different topological phases of the TB model for  $\hat{m}(\theta, \phi)$  are summarized in Fig. 2. The first BZ with high-symmetry points  $M_i$  ( $M_1, M_2, M_3$ ) and  $K_i$  ( $K_1, K_2, K_3$ ) are shown in Fig. 2(a).

As argued based on symmetry considerations that the R-SOC induces Chern insulating phases for  $\hat{m}(\theta = 90^\circ, \phi)$ . In this case, the topological phase diagram is shown in Fig. 2(b). The TPT is signalled by the closing of gaps at specific in-plane moment orientations, such as  $\phi = 0^\circ, 60^\circ, 120^\circ$  and their inverted counterparts with respect to the  $\Gamma$  point at  $\phi = 180^\circ, 240^\circ, 300^\circ$  (this set of angles are denoted as  $\{\phi_C\}$ ) due to the protection of in-plane mirror symmetry. When the in-plane orientation of the moments traverse through the above symmetry pro-

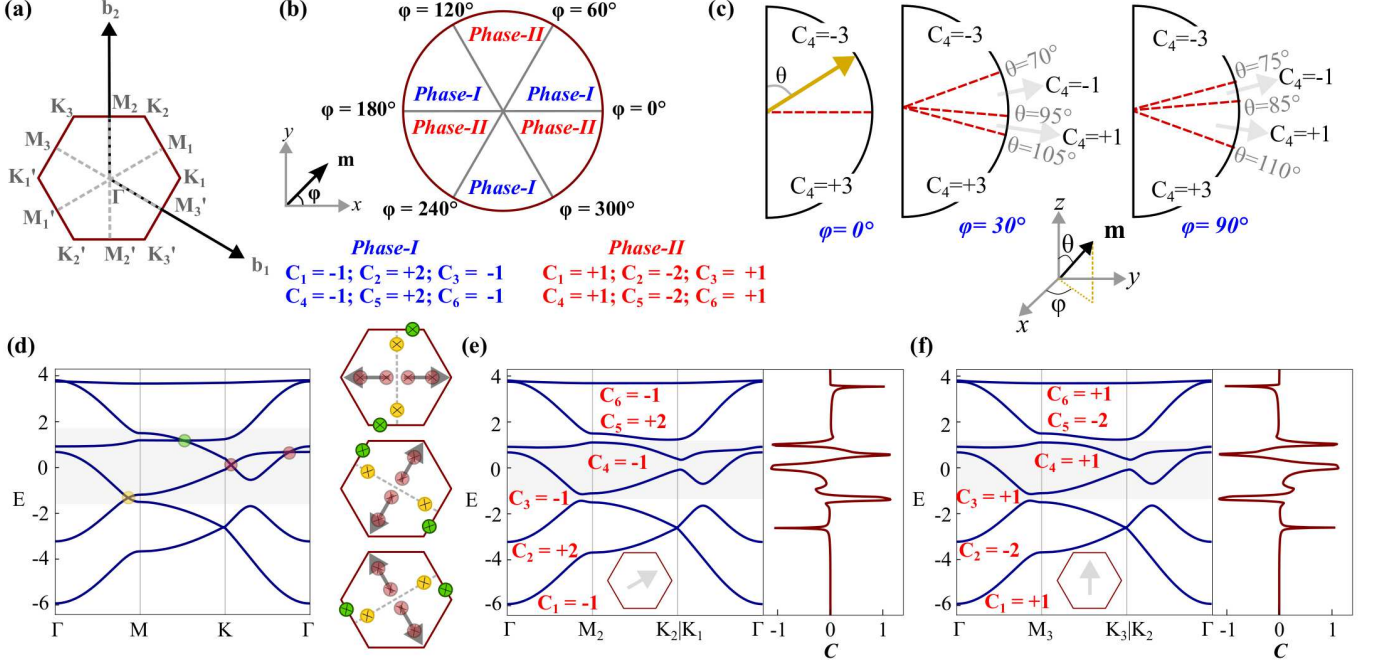


FIG. 2. Topological properties of the TB Hamiltonian with parameters  $t = 1.0$ ,  $B = 1.5t$ ,  $t_I = 0.2t$ , and  $t_R = 0.5t$ . (a) First BZ of the kagome lattice with in-plane mirrors (grey dotted lines) and distinct high-symmetry points. (b) Topological phase diagram showing the Chern number  $C$  for different bands as a function of  $\hat{m}(\theta = 90^\circ, \phi)$ . (c) TPT of the fourth band due to the variation of  $\hat{m}(\theta, \phi = \text{constant})$  for  $\phi = 0^\circ, 30^\circ$  and  $90^\circ$ . (d) Band-crossing points due to ferromagnetic moment alignments  $\hat{m}(\theta = 90^\circ, \phi)$  for  $\phi \in \{\phi_C\}$  indicating TPT. (e) Band structure and Chern number  $C$  for each band at  $\hat{m}(\theta = 90^\circ, \phi = 30^\circ)$ , where the absence of mirror symmetry results in nonzero Chern numbers for all bands. (f) Same as (e), but for  $\hat{m}(\theta = 90^\circ, \phi = 90^\circ)$ , where the TPT reverses the Chern numbers compared to (e).

tected phases, the Chern number  $C$  of each band flips, giving rise to two distinct phases, phase-I and phase-II as shown in Fig. 2(b) where the kagome bands are numbered from 1 to 6 from bottom to top.

TPT are also observed for the variation of  $\hat{m}(\theta, \phi = \text{constant})$ . These transitions arise from the competition between I-SOC and R-SOC, captured by two distinct parameters  $t_I$  and  $t_R$ , in the TB model. In the absence of R-SOC ( $t_R = 0$ ), TPT only occur at  $\hat{m}(\theta = 90^\circ, \phi)$  respecting the aforementioned symmetries and the Onsager relation<sup>1,25</sup>.

Inclusion of R-SOC ( $t_R \neq 0$ ) produces a rich topological phase diagram as illustrated in Fig. 2(c). Here the component of the moment parallel to the kagome plane ( $\theta = 90^\circ$ ) influences topology through  $t_R$ , while the perpendicular component ( $\theta = 0^\circ$ ) does it through  $t_I$ . We note when  $\phi$  does not belong to  $\{\phi_C\}$ , there are several TPT mediated by the competition between  $t_R$  and  $t_I$  as the orientation of the moment changes from  $\theta = 0^\circ$  to  $\theta = 180^\circ$  for a constant  $\phi$ . These transitions are shown in Fig. 2(c) for  $\phi = 0^\circ, 30^\circ$  and  $90^\circ$ , focusing on the fourth kagome band, having the highest Chern number,  $C_4 = \pm 3$ , for  $\hat{m}(\theta, \phi = \text{constant})$ . In addition, our analysis reveals that if a phase transition occurs at  $(\theta, \phi)$ , it also takes place at  $(180^\circ - \theta, \phi + 60^\circ)$ , uncovering a symmetry in the phase diagram. Using this property and Onsager relation, the complete topological phase diagram of

the TB model can be constructed.

We now focus on the band structure due to in-plane moment variations ( $\hat{m}(\theta = 90^\circ, \phi)$ ). When the direction of moments are perpendicular to the in-plane mirrors, the protected mirror symmetry forces all bands to touch, resulting in the absence of band gap, as shown in Fig. 2(d). The band crossing points (Weyl points) vary depending on the specific in-plane mirror symmetry being preserved. For example, for  $\phi = 0^\circ$ , band touching occurs along the  $\Gamma - M_2 - K_2$  and  $K_1 - \Gamma$  paths; while for  $\phi = 60^\circ$ , it occurs along  $\Gamma - M_3 - K_3$  and  $K_2 - \Gamma$  paths. All possible phase transition points for different in-plane moment orientations are shown in Fig. 2(d). The variation of in-plane moments results in a non-trivial Chern number for each band, as shown in Fig. 2(e) and (f) for two different moment orientations of  $\hat{m}(\theta = 90^\circ, \phi = 30^\circ)$  and  $\hat{m}(\theta = 90^\circ, \phi = 90^\circ)$  respectively where the changes in Chern numbers occur due to the topological transition at  $\phi = 60^\circ \in \{\phi_C\}$ .

*Material realization.*— We shall illustrate that our analysis of the topological properties of a 2D ferromagnetic kagome system based on a simple TB model with one orbital per site will provide valuable insights to understand the topological properties of a real ferromagnetic kagome monolayer with broken out-of-plane mirror symmetry. In view of the above, we have considered the ferromagnetic kagome monolayer  $\text{Co}_3\text{Pb}_3\text{S}_2$  with space group P-3m1



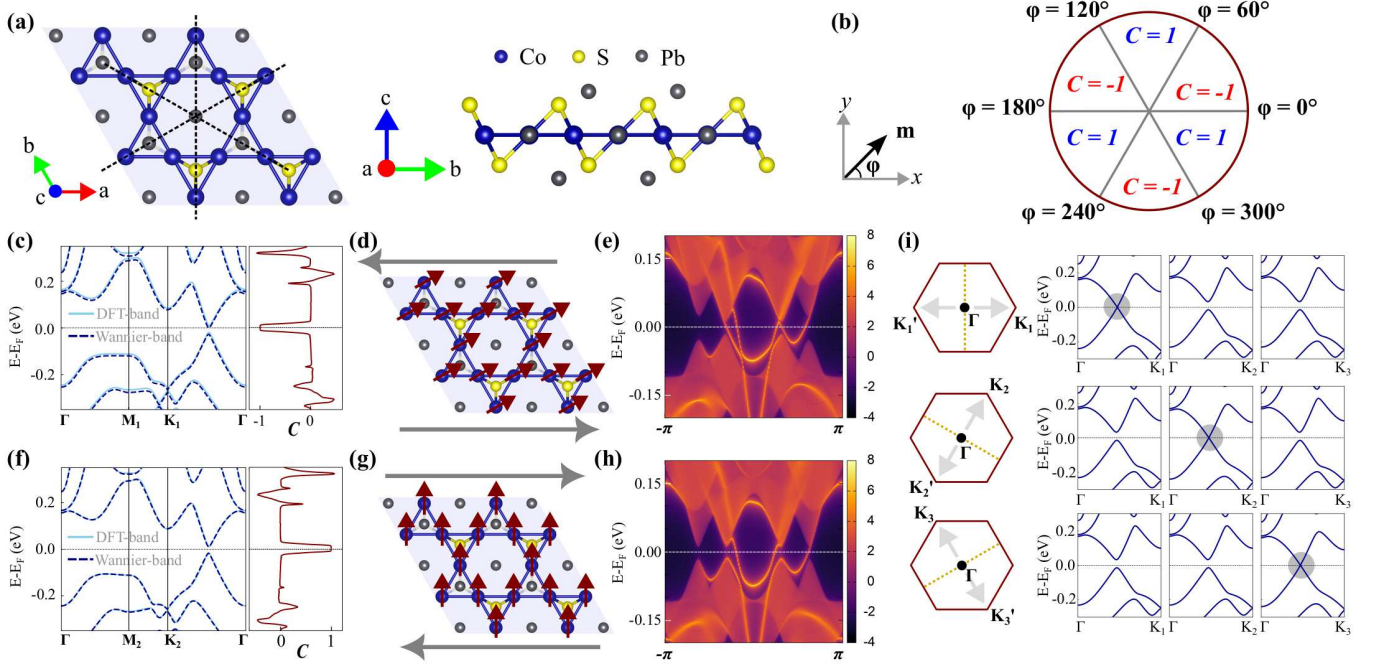


FIG. 3. Topological properties of the ferromagnetic  $\text{Co}_3\text{Pb}_3\text{S}_2$  monolayer under in-plane moment variation. (a) Crystal structure showing in-plane mirrors (black dotted lines) and broken out-of-plane mirror symmetry (light-blue plane, coinciding with the kagome plane). (b) Topological phase diagram for in-plane moment variation ( $\theta = 90^\circ$ ). (c) Electronic band structure for  $\hat{m}(\theta = 90^\circ, \phi = 30^\circ)$ , with a Chern number  $C = -1$  at  $E_F$ . (d) Edge states for  $\hat{m}(\theta = 90^\circ, \phi = 30^\circ)$ , with edge cuts perpendicular to the crystallographic axis  $\vec{b}$ . (e) Top-edge spectral function confirming  $C = -1$  for the same edge cut. (f)–(h) Corresponding results for  $\hat{m}(\theta = 90^\circ, \phi = 90^\circ)$  with  $C = +1$ . (i) TPT for in-plane moment variation ( $\theta = 90^\circ$ ), occurring cyclically at  $\phi = 0^\circ, 60^\circ$ , and  $120^\circ$ , and their equivalents at  $\phi = 180^\circ, 240^\circ$ , and  $300^\circ$ , tied to different  $\Gamma$ - $K$  paths parallel to the moment directions.

(No. 164) belonging to the family  $\text{Co}_3\text{X}_3\text{Y}_2$  ( $X=\text{Sn, Pb}$ ;  $Y=\text{S, Se}$ )<sup>26–28</sup> as a representative compound.

DFT calculations were performed using the plane-wave-based projector augmented wave (PAW) method implemented in the Vienna *ab initio* simulation package (VASP) with the generalized gradient approximation for exchange-correlation<sup>29–31</sup>. The plane-wave cutoff was set to 500 eV, and a  $\Gamma$ -centered  $12 \times 12 \times 1$  k-point mesh was used for BZ integration. Constrained-moment calculations fixed the Co-moment directions, while the Wannier90 and WannierTools codes were employed to construct the numerical TB model retaining Co-d and Pb-p orbitals in the basis to analyse the topological properties of the chosen material<sup>32–34</sup>.

The kagome structure of  $\text{Co}_3\text{Pb}_3\text{S}_2$ , featuring in-plane mirrors and broken out-of-plane mirror symmetry, is shown in Fig. 3(a). While the magnetic ground state is an easy-axis ferromagnet with moment  $\approx 0.4\mu_B$  per Co, the magnetic anisotropy energy between the easy-axis and in-plane ferromagnetic orientation (along the  $x$ -axis) is 1.3 meV, suggesting that the moment orientations may be experimentally achieved using external fields<sup>35</sup>. The topological phase diagram for varying in-plane moment orientations is presented in Fig. 3(b), showing that the Chern number  $C$  calculated for bands till  $E_F$  varies between  $-1$  and  $+1$ , consistent with the

TB model (Fig. 2(b)).

For an in-plane moment orientation at  $\hat{m}(\theta = 90^\circ, \phi = 30^\circ)$ , detailed results are shown in Fig. 3(c) to (e). The band-gap is calculated to be 85 meV. The variation of the Chern number  $C$  near  $E_F$  is shown in Fig. 3(c). Finite edge cuts (Fig. 3(d)) yield the surface spectrum of the top edge (Fig. 3(e)), supporting the  $C = -1$  phase. Similarly results for  $C = +1$ , when the in-plane moment is along  $\hat{m}(\theta = 90^\circ, \phi = 90^\circ)$  is shown in Fig. 3(f) to (h). The TPT due to in-plane moment orientations occur for  $\phi \in \{\phi_C\}$  when the moments are perpendicular to the in-plane mirrors, as in the TB model. At these points, conduction and valence bands touch at points along specific  $\Gamma$ - $K$  paths, which are perpendicular to the respective in-plane mirror planes where mirror symmetry is preserved, as shown in Fig. 3(i)<sup>15</sup>.

The ground state of the monolayer  $\text{Co}_3\text{Pb}_3\text{S}_2$  is an easy-axis ferromagnet with a Chern number  $C = +3$ <sup>27</sup>, and our calculation reveal that it exhibit TPT upon the variation of the polar angle of the magnetic moment  $\hat{m}(\theta, \phi = \text{constant})$ . These transitions, shown for selected  $\phi$  values in Fig. 4, closely resemble the results of the TB model (Fig. 2(c)). A notable difference is that in the TB model, the band gap closes along various high-symmetry paths, whereas in the material, gap-closing is restricted only along  $\Gamma$ - $K$  directions.

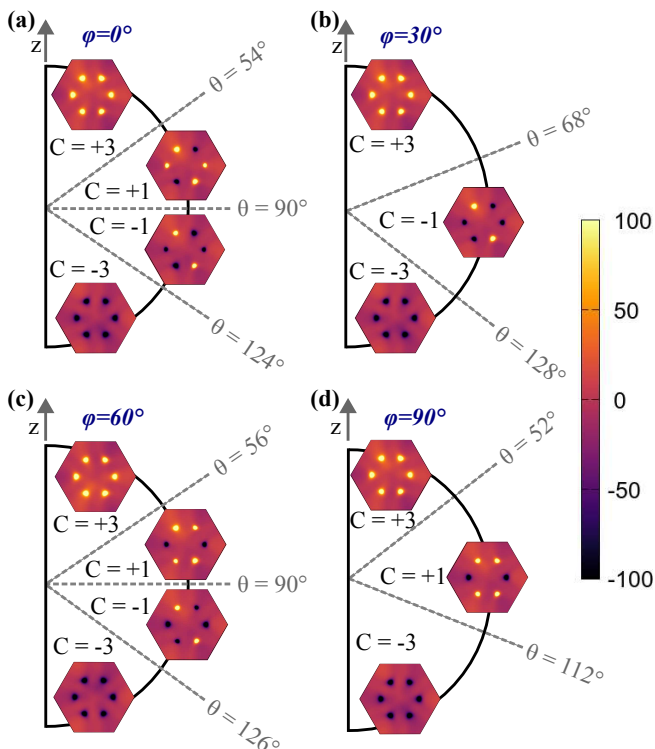


FIG. 4. TPT and Berry curvature of the top valence band within the first BZ for the ferromagnetic  $\text{Co}_3\text{Pb}_3\text{S}_2$  monolayer under variation of moment  $\hat{m}(\theta, \phi = \text{constant})$  for (a)  $\phi = 0^\circ$ , (b)  $\phi = 30^\circ$ , (c)  $\phi = 60^\circ$ , and (d)  $\phi = 90^\circ$ .

The locations of these gap-closing points for  $\hat{m}(\theta, \phi = \text{constant})$  are linked to the Berry curvature  $\Omega_z(\vec{k})$ , which exhibits peaks along all  $\Gamma$ - $K$  paths in the first BZ<sup>28</sup> (see Fig. 4). In the ground state  $\hat{m}(\theta = 0^\circ)$ , six positive peaks in  $\Omega_z(\vec{k})$  reflect the Chern number  $C = +3$ . Due to the variation of  $\hat{m}(\theta, \phi = 0^\circ)$ , the first TPT occurs at  $\theta = 54^\circ$  along the  $K_2$ - $\Gamma$ - $K'_2$  path, signaled by the reversal of  $\Omega_z(\vec{k})$  peaks along this path.

Since the TPT at  $54^\circ$  is characterized by two Weyl points, therefore  $C$  decreases by 2, as shown in Fig. 4(a). Similar argument holds for all of the TPT shown in Fig. 4(a) to (d)<sup>28</sup> for  $\phi = 0^\circ, 30^\circ, 60^\circ$  and  $90^\circ$  respectively.

All the topological phase transition points obey the relation  $(\theta, \phi) \rightarrow (180^\circ - \theta, \phi + 60^\circ)$  (see Fig. 4), confirming the robustness of the simple TB model in explaining the material-specific DFT results. However, a key limitation of the TB model is its inability to capture additional TPT occurring at  $\hat{m}(\theta \neq 90^\circ, \phi \in \{\phi_C\})$  as illustrated in Fig. 4(a) and (c) in contrast to Fig. 2(c) for  $\phi = 0^\circ$  due to the presence of more complex band dispersion in real materials.

*Summary.*— In this work, we demonstrate that in-plane ferromagnetic Chern insulating phases and consequent TPT can also be realized in kagome materials, analogous to honeycomb systems<sup>15</sup> where, R-SOC arising from broken out-of-plane mirror symmetry play a crucial role for the topological behavior. Specific in-plane moment orientations  $\hat{m}(\theta = 90^\circ, \phi \in \{\phi_C\})$  that preserve the in-plane mirror symmetries lead to rich topological phase diagram for  $\hat{m}(\theta = 90^\circ, \phi)$ . Further we have shown that the TPT driven by variations of  $\hat{m}(\theta, \phi = \text{constant})$  results from a competition between R-SOC and I-SOC. In the absence of R-SOC, the TPT for  $\hat{m}(\theta, \phi = \text{constant})$  only occur at  $\theta = 90^\circ$  with the Chern number changing its sign following the Onsager relation. Inclusion of R-SOC introduces additional features, giving rise to a richer landscape of Chern insulating phases, as confirmed by our DFT calculations. All these phases that could potentially be realized experimentally by application of external fields, will be important for applications in quantum technology.

*Acknowledgements.*— R.D thanks the Council of Scientific and Industrial Research (CSIR), India for research fellowship (File No. 09/080(1171)/2020-EMR-I). I.D would like to thank the Science and Engineering Research Board (SERB) India (Project No. CRG/2021/003024) and Technical Research Center, Department of Science and Technology Government of India for support.

- [1] L. Šmejkal, A. H. MacDonald, J. Sinova, S. Nakatsuji, and T. Jungwirth, Anomalous hall antiferromagnets, *Nature Reviews Materials* **7**, 482 (2022).
- [2] V. Bonbien, F. Zhuo, A. Salimath, O. Ly, A. Abbout, and A. Manchon, Topological aspects of antiferromagnets, *Journal of Physics D: Applied Physics* **55**, 103002 (2021).
- [3] Q. Wang, H. Lei, Y. Qi, and C. Felser, Topological quantum materials with kagome lattice, *Accounts of Materials Research* **5**, 786 (2024).
- [4] K. Ohgushi, S. Murakami, and N. Nagaosa, Spin anisotropy and quantum hall effect in the kagomé lattice: Chiral spin state based on a ferromagnet, *Phys. Rev. B* **62**, R6065 (2000).
- [5] Z.-Y. Zhang, The quantum anomalous hall effect in kagomé lattices, *Journal of Physics: Condensed Matter* **23**, 365801 (2011).
- [6] M. Z. Hasan and C. L. Kane, Colloquium: Topological insulators, *Rev. Mod. Phys.* **82**, 3045 (2010).
- [7] Q. L. He, T. L. Hughes, N. P. Armitage, Y. Tokura, and K. L. Wang, Topological spintronics and magnetoelectronics, *Nature Materials* **21**, 15 (2022).
- [8] J.-X. Yin, B. Lian, and M. Z. Hasan, Topological kagome magnets and superconductors, *Nature* **612**, 647 (2022).
- [9] F. D. M. Haldane, Model for a quantum hall effect without landau levels: Condensed-matter realization of the "parity anomaly", *Phys. Rev. Lett.* **61**, 2015 (1988).
- [10] Y. Zhang and C. Zhang, Quantized anomalous hall insulator in a nanopatterned two-dimensional electron gas, *Phys. Rev. B* **84**, 085123 (2011).
- [11] Y. Ren, J. Zeng, X. Deng, F. Yang, H. Pan, and Z. Qiao, Quantum anomalous hall effect in atomic crystal layers from in-plane magnetization,

- Phys. Rev. B **94**, 085411 (2016).
- [12] X.-L. Sheng and B. K. Nikolić, Monolayer of the  $5d$  transition metal trichloride  $\text{oscl}_3$ : A playground for two-dimensional magnetism, room-temperature quantum anomalous hall effect, and topological phase transitions, Phys. Rev. B **95**, 201402 (2017).
- [13] J.-Y. You, Z. Zhang, B. Gu, and G. Su, Two-dimensional room-temperature ferromagnetic semiconductors with quantum anomalous hall effect, Phys. Rev. Appl. **12**, 024063 (2019).
- [14] Z. Li, Y. Han, and Z. Qiao, Chern number tunable quantum anomalous hall effect in monolayer transitional metal oxides via manipulating magnetization orientation, Phys. Rev. Lett. **129**, 036801 (2022).
- [15] R. Das, S. Bandyopadhyay, and I. Dasgupta, In-plane magnetization orientation driven topological phase transition in  $\text{oscl}_3$  monolayer, Electronic Structure **6**, 025005 (2024).
- [16] L. Zhang, H. Chen, J. Ren, and X. Yuan, The quantum anomalous hall effect in two-dimensional hexagonal monolayers studied by first-principles calculations, iScience **28**, 111622 (2025).
- [17] M. P. Ghimire, J. I. Facio, J.-S. You, L. Ye, J. G. Checkelsky, S. Fang, E. Kaxiras, M. Richter, and J. van den Brink, Creating weyl nodes and controlling their energy by magnetization rotation, Phys. Rev. Res. **1**, 032044 (2019).
- [18] A. Ozawa, K. Kobayashi, and K. Nomura, Effective model analysis of intrinsic spin hall effect with magnetism in the stacked kagome weyl semimetal  $\text{co}_3\text{sn}_2\text{s}_2$ , Phys. Rev. Appl. **21**, 014041 (2024).
- [19] X. Liu, H.-C. Hsu, and C.-X. Liu, In-plane magnetization-induced quantum anomalous hall effect, Phys. Rev. Lett. **111**, 086802 (2013).
- [20] D. I. Khomskii, *Transition Metal Compounds* (Cambridge University Press, 2014).
- [21] H. Chen, Q. Niu, and A. H. MacDonald, Anomalous hall effect arising from noncollinear antiferromagnetism, Phys. Rev. Lett. **112**, 017205 (2014).
- [22] A. Bolens and N. Nagaosa, Topological states on the breathing kagome lattice, Phys. Rev. B **99**, 165141 (2019).
- [23] J. Watanabe, Y. Araki, K. Kobayashi, A. Ozawa, and K. Nomura, Magnetic orderings from spin-orbit coupled electrons on kagome lattice, Journal of the Physical Society of Japan **91**, 083702 (2022), <https://doi.org/10.7566/JPSJ.91.083702>.
- [24] C. L. Kane and E. J. Mele, Quantum spin hall effect in graphene, Phys. Rev. Lett. **95**, 226801 (2005).
- [25] L. D. Landau and E. M. Lifshitz, *Electrodynamics of Continuous Media* (Pergamon, New York, 1984).
- [26] L. Muechler, E. Liu, J. Gayles, Q. Xu, C. Felser, and Y. Sun, Emerging chiral edge states from the confinement of a magnetic weyl semimetal in  $\text{co}_3\text{sn}_2\text{s}_2$ , Phys. Rev. B **101**, 115106 (2020).
- [27] Z. Zhang, J.-Y. You, X.-Y. Ma, B. Gu, and G. Su, Kagome quantum anomalous hall effect with high chern number and large band gap, Phys. Rev. B **103**, 014410 (2021).
- [28] K. Nakazawa, Y. Kato, and Y. Motome, Topological transitions by magnetization rotation in kagome monolayers of the ferromagnetic weyl semimetal co-based shandite, Phys. Rev. B **110**, 085112 (2024).
- [29] P. E. Blöchl, Projector augmented-wave method, Phys. Rev. B **50**, 17953 (1994).
- [30] G. Kresse and J. Hafner, Ab initio molecular dynamics for liquid metals, Phys. Rev. B **47**, 558 (1993).
- [31] J. P. Perdew, K. Burke, and M. Ernzerhof, Generalized gradient approximation made simple, Phys. Rev. Lett. **77**, 3865 (1996).
- [32] G. Pizzi, V. Vitale, R. Arita, S. Blügel, F. Freimuth, G. Géranton, M. Gibertini, D. Gresch, C. Johnson, T. Koretsune, J. Ibañez-Azpiroz, H. Lee, J.-M. Lihm, D. Marchand, A. Marrazzo, Y. Mokrousov, J. I. Mustafa, Y. Nohara, Y. Nomura, L. Paulatto, S. Poncé, T. Ponweiser, J. Qiao, F. Thöle, S. S. Tsirkin, M. Wierzbowska, N. Marzari, D. Vanderbilt, I. Souza, A. A. Mostofi, and J. R. Yates, Wannier90 as a community code: new features and applications, Journal of Physics: Condensed Matter **32**, 165902 (2020).
- [33] N. Marzari, A. A. Mostofi, J. R. Yates, I. Souza, and D. Vanderbilt, Maximally localized wannier functions: Theory and applications, Rev. Mod. Phys. **84**, 1419 (2012).
- [34] Q. Wu, S. Zhang, H.-F. Song, M. Troyer, and A. A. Soluyanov, Wanniertools: An open-source software package for novel topological materials, Computer Physics Communications **224**, 405 (2018).
- [35] N. Kumar, Y. Soh, Y. Wang, J. Li, and Y. Xiong, Tuning the electronic band structure in a kagome ferromagnetic metal via magnetization, Phys. Rev. B **106**, 045120 (2022).